Journal of Computational Physics **161,** 680–699 (2000)
doi:10.1006/jcph.2000.6522, available online at http://www.idealibrary.com on IDEAL®

Lattice Boltzmann Method for 3-D Flows with Curved Boundary

Renwei Mei,* Wei Shyy,* Dazhi Yu,* and Li-Shi Luo†

*Department of Aerospace Engineering, Mechanics & Engineering Science, University of Florida, Gainesville, Florida 32611-6250; and †ICASE, MS 132C, NASA Langley Research Center, 3 West Reid Street, Building 1152, Hampton, Virginia 23681-2199
E-mail: rwm@aero.ufl.edu, wei-shyy@ufl.edu, ydz@aero.ufl.edu, luo@icase.edu

Received September 20, 1999; revised March 13, 2000

In this work, we investigate two issues that are important to computational efficiency and reliability in fluid dynamic applications of the lattice Boltzmann equation (LBE): (1) Computational stability and accuracy of different lattice Boltzmann models and (2) the treatment of the boundary conditions on curved solid boundaries and their 3-D implementations. Three athermal 3-D LBE models (Q15D3, Q19D3, and Q27D3) are studied and compared in terms of efficiency, accuracy, and robustness. The boundary treatment recently developed by Filippova and Hänel (1998, *J. Comp. Phys.* **147**, 219) and Mei *et al.* (1999, *J. Comp. Phys.* **155**, 307) in 2-D is extended to and implemented for 3-D. The convergence, stability, and computational efficiency of the 3-D LBE models with the boundary treatment for curved boundaries were tested in simulations of four 3-D flows: (1) Fully developed flows in a square duct, (2) flow in a 3-D lid-driven cavity, (3) fully developed flows in a circular pipe, and (4) a uniform flow over a sphere. We found that while the 15-velocity 3-D (Q15D3) model is more prone to numerical instability and the Q27D3 is more computationally intensive, the Q19D3 model provides a balance between computational reliability and efficiency. Through numerical simulations, we demonstrated that the boundary treatment for 3-D arbitrary curved geometry has second-order accuracy and possesses satisfactory stability characteristics.

Key Words: lattice Boltzmann equation; boundary condition for curved geometries; accuracy; 3-D flows.

I. INTRODUCTION

1.1. *Basic Notion of the Lattice Boltzmann Equation*

In one fashion or another, conventional methods of computational fluid dynamics (CFD) compute pertinent flow fields, such as velocity $\boldsymbol{u}$ and pressure p, by numerically solving the

0021-9991/00 $35.00

Navier–Stokes equations in space $\boldsymbol{x}$ and time t [1–3]. In contrast, various kinetic methods use the transport equation, or the Boltzmann equation in particular, for various problems in fluid dynamics. The Boltzmann equation deals with the single particle distribution function $f(\boldsymbol{x}, \xi, t)$, where ξ is the particle velocity, in phase space $(\boldsymbol{x}, \xi)$ and time t. Recently, the method of the lattice Boltzmann equation (LBE) [4–7] has become an alternative to the conventional CFD methods employing Navier–Stokes equations. The theoretical premises of the LBE method are that (1) hydrodynamics is insensitive to the details of microscopic physics, and (2) hydrodynamics can be preserved so long as the conservation laws and associated symmetries are respected in the microscopic or mesoscopic level. Therefore, the computational advantages of the LBE method are attained by drastically reducing the particle velocity space ξ to only a very few discrete points without seriously degrading hydrodynamics. This is possible because the LBE method rigorously preserves the hydrodynamic moments of the distribution function f, such as mass density and momentum fluxes, and the necessary symmetries [8–10].

One popular kinetic model is the Boltzmann equation with the single relaxation time approximation [11],

$$\frac{\partial f}{\partial t} + \xi \cdot \nabla f = -\frac{1}{\lambda}\left[f - f^{(0)}\right], \tag{1}$$

where ξ is the particle velocity, $f^{(0)}$ is the equilibrium distribution function (the Maxwell–Boltzmann distribution function), and λ is the relaxation time. The mass density ρ and momentum density $\rho\boldsymbol{u}$ are the first $(D+1)$ hydrodynamic moments of the distribution function f and $f^{(0)}$, where D is the dimension of velocity space.

To solve for f numerically, Eq. (1) is first discretized in the velocity space ξ using a finite set of velocities $\{\xi_\alpha\}$ without affecting the conserved hydrodynamic moments [9–11],

$$\frac{\partial f_\alpha}{\partial t} + \xi_\alpha \cdot \nabla f_\alpha = -\frac{1}{\lambda}\left[f_\alpha - f_\alpha^{(\mathrm{eq})}\right]. \tag{2}$$

In the above equation, $f_\alpha(\boldsymbol{x}, t) \equiv f(\boldsymbol{x}, \xi_\alpha, t)$ and $f_\alpha^{(\mathrm{eq})} = f^{(0)}(\boldsymbol{x}, \xi_\alpha, t)$ are the distribution function and the equilibrium distribution function of the αth discrete velocity ξ_α, respectively. The 9-velocity (or 9-bit) LBE model on the 2-D square lattice, denoted as the Q9D2 model, has been widely used for simulating 2-D flows. For 3-D flows, there are several cubic lattice models, such as the 15-bit (Q15D3), 19-bit (Q19D3), and 27-bit (Q27D3) models [12], which have been used in the literature. All three models have a rest particle (with zero velocity) in the discretized velocity set $\{\xi_\alpha\}$. A minor variation of those models is to remove the rest particles from the discrete velocity set; the resulting models are known as the Q14D3, Q18D3, and Q26D3 models, respectively. The LBE models with a rest particle generally have better computational stability. For athermal fluids, the equilibrium distributions for the Q9D2, Q15D3, Q19D3, and Q27D3 models are all of the form [9]

$$f_\alpha^{(\mathrm{eq})} = \rho w_\alpha \left[1 + \frac{3}{c^2}\boldsymbol{e}_\alpha \cdot \boldsymbol{u} + \frac{9}{2c^4}(\boldsymbol{e}_\alpha \cdot \boldsymbol{u})^2 - \frac{3}{2c^2}\boldsymbol{u} \cdot \boldsymbol{u}\right], \tag{3}$$

where w_α is a weighting factor and $\boldsymbol{e}_\alpha$ is a discrete velocity, $c = \delta x/\delta t$ is the lattice speed, and δx and δt are the lattice constant and the time step, respectively. (The values of the weighting factor w_α for the Q15D3, Q19D3, and Q27D3 models and the diagrams illustrating the lattice structures for the Q15D3 and Q19D3 models are given in the Appendix.) It can be shown that

$f_\alpha^{(\mathrm{eq})}$ is in fact a Taylor series expansion of the Maxwellian $f^{(0)}$ [8, 9]. This approximation of $f^{(0)}$ by the above $f_\alpha^{(\mathrm{eq})}$ makes the method valid only in the incompressible limit $u/c \to 0$.

With the velocity space discretized, the hydrodynamic moments of f and $f^{(0)}$ are evaluated by the following quadrature formulas:

$$\rho = \sum_\alpha f_\alpha = \sum_\alpha f_\alpha^{(\mathrm{eq})}, \tag{4a}$$

$$\rho \boldsymbol{u} = \sum_\alpha \boldsymbol{e}_\alpha f_\alpha = \sum_\alpha \boldsymbol{e}_\alpha f_\alpha^{(\mathrm{eq})}. \tag{4b}$$

The speed of sound of the above 3-D LBE models is $c_s = c/\sqrt{3}$ and the equation of state is that of an ideal gas $p = \rho c_s^2$. The viscosity of the fluid is $\nu = \lambda c_s^2$.

Equation (2) is often discretized in space, $\boldsymbol{x}$, and time, t, into

$$f_\alpha(\boldsymbol{x}_i + \boldsymbol{e}_\alpha \delta t, t + \delta t) - f_\alpha(\boldsymbol{x}_i, t) = -\frac{1}{\tau}\left[f_\alpha(\boldsymbol{x}_i, t) - f_\alpha^{(\mathrm{eq})}(\boldsymbol{x}_i, t)\right], \tag{5}$$

where $\tau = \lambda/\delta t$. This is the lattice Boltzmann equation with the Bhatnagar–Gross–Krook (BGK) approximation [11] and is often referred to as the LBGK model [4, 5]. The viscosity in the NS equation derived from Eq. (5) is

$$\nu = (\tau - 1/2) c_s^2 \delta t. \tag{6}$$

This choice for the viscosity makes the LBGK scheme formally a second order method for solving incompressible flows [9]. The positivity of the viscosity requires that $\tau > 1/2$. Equation (6) can be solved in the following two steps:

$$\text{collision step:} \quad \tilde{f}_\alpha(\boldsymbol{x}_i, t) = f_\alpha(\boldsymbol{x}_i, t) - \frac{1}{\tau}\left[f_\alpha(\boldsymbol{x}_i, t) - f_\alpha^{(\mathrm{eq})}(\boldsymbol{x}_i, t)\right], \tag{7a}$$

$$\text{streaming step:} \quad f_\alpha(\boldsymbol{x}_i + \boldsymbol{e}_\alpha \delta t, t + \delta t) = \tilde{f}_\alpha(\boldsymbol{x}_i, t), \tag{7b}$$

where $\tilde{f}_\alpha$ denotes the post-collision state of the distribution function. It is noted that the collision step is completely local, and the streaming step is uniform and requires little computational effort. Equation (7) is explicit, easy to implement, and straightforward to parallelize.

1.2. *Boundary Condition on a Solid Surface*

To date, most Neumann-type boundary conditions for a solid boundary used in the LBE method are based upon the bounce-back boundary condition: A particle colliding with a stationary wall simply reverses its momentum. Much of the previous work on LBE boundary conditions is devoted to the analysis and improvement of the bounce-back boundary condition [13–21, 27]. The bounce-back boundary condition can attain second-order accuracy if the boundary is fictictiously placed halfway between two nodes. That is, the second-order accuracy of the bounce-back boundary condition can only be achieved when the boundaries are located right in the middle of two neighboring lattices [$\Delta = 0.5$; see Eq. (8)]. (Readers are referred to our recent work [22] for a summary of the previous work.) This prevents the direct application of the bounce-back–type boundary conditions to simulate a solid

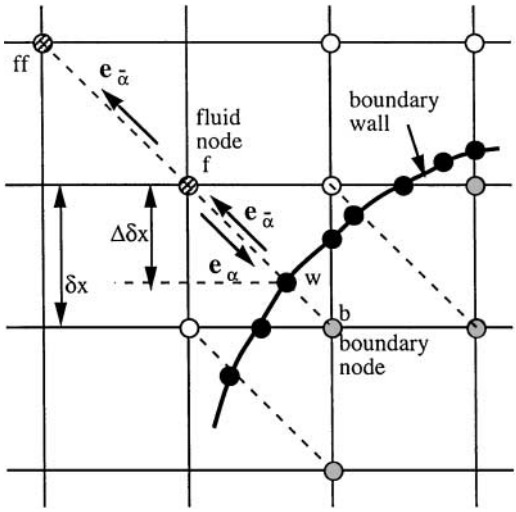

FIG. 1. 2-D projection of the layout of the regularly spaced lattices and curved wall boundary.

body with smooth curvature. To circumvent this difficulty, Mei and Shyy solved Eq. (2) in curvilinear coordinates using a finite difference method to solve for $\tilde{f}_\alpha$ [28]. One can also use body-fitted curvilinear coordinates with interpolation throughout the entire mesh, except at the boundaries where the bounce-back boundary condition is used [29]. In more recent works [22, 23], Cartesian coordinates are adopted with interpolation used only at the boundaries. These techniques rely on the freedom of using interpolation techniques. We used the latter technique in the present work.

As shown in Fig. 1 for a 2-D projection involving a 3-D body, the streaming step requires the knowledge of $\tilde{f}_{\bar{\alpha}}(\boldsymbol{x}_b, t)$, in which $\boldsymbol{e}_{\bar{\alpha}} = -\boldsymbol{e}_\alpha$, at $\boldsymbol{x}_b$ on the solid side in order to obtain $f_{\bar{\alpha}}(\boldsymbol{x}_f, \delta t)$ for the lattice node located on the fluid side at $\boldsymbol{x}_f = \boldsymbol{x}_b + \boldsymbol{e}_{\bar{\alpha}}\delta t$. Defining

$$\Delta = \frac{|\boldsymbol{x}_f - \boldsymbol{x}_w|}{|\boldsymbol{x}_f - \boldsymbol{x}_b|} \tag{8}$$

as the fraction of an intersected link in the fluid region, it is seen that $0 \le \Delta \le 1$ and the horizontal or vertical distance between $\boldsymbol{x}_b$ and $\boldsymbol{x}_w$ is $(1 - \Delta)\delta x$ on the cubic lattice.

Based on the work of Filippova and Hänel [23], hereinafter referred to as FH, Mei *et al.* [22] proposed the following treatment for $\tilde{f}_{\bar{\alpha}}(\boldsymbol{x}_b, t)$ on curved boundaries:

$$\tilde{f}_{\bar{\alpha}}(\boldsymbol{x}_b, t) = (1 - \chi)\,\tilde{f}_\alpha(\boldsymbol{x}_f, t) + \chi\, f_\alpha^{(*)}(\boldsymbol{x}_b, t) + 2w_\alpha\rho\frac{3}{c^2}\boldsymbol{e}_{\bar{\alpha}} \cdot \boldsymbol{u}_w \tag{9}$$

with

$$f_\alpha^{(*)}(\boldsymbol{x}_b, t) = w_\alpha\rho(\boldsymbol{x}_f, t)\left[1 + \frac{3}{c^2}\boldsymbol{e}_\alpha \cdot \boldsymbol{u}_{bf} + \frac{9}{2c^4}(\boldsymbol{e}_\alpha \cdot \boldsymbol{u}_f)^2 - \frac{3}{2c^2}\boldsymbol{u}_f \cdot \boldsymbol{u}_f\right] \tag{10}$$

and

$$\boldsymbol{u}_{bf} = (\Delta - 1)\boldsymbol{u}_f/\Delta + \boldsymbol{u}_w/\Delta \quad \text{and} \quad \chi = (2\Delta - 1)/\tau \qquad \text{for } \Delta \ge 1/2 \tag{11}$$

$$\boldsymbol{u}_{bf} = \boldsymbol{u}_{ff} = \boldsymbol{u}_f(\boldsymbol{x}_f + \boldsymbol{e}_{\bar{\alpha}}\delta t, t) \quad \text{and} \quad \chi = (2\Delta - 1)/(\tau - 2) \qquad \text{for } \Delta < 1/2. \tag{12}$$

It is noted that Eq. (12) for $\boldsymbol{u}_{bf}$ and χ differs from that originally proposed by FH. The choice for $\boldsymbol{u}_{bf}$ given by Eq. (12) improves the computational stability for $\tau < 1$ and $\Delta < 1/2$ [22]. Since Eqs. (9)–(12) are in vector form, they can be directly extended to 3-D flows with curved boundaries.

1.3. *Scope of the Present Work*

The present study examines two issues in 3-D incompressible fluid dynamics simulations with arbitrary boundaries using the LBE method: (i) The performance of various 3-D athermal LBE models for viscous flows, and (ii) the efficacy and reliability of the extension of the curved boundary treatment from 2-D to 3-D flows. We focus on the stability and accuracy of the computation and the robustness in handling an arbitrary curved geometry. In Section II, a modification of the choice of $\boldsymbol{u}_{bf}$ and the expression for χ when $\Delta \geq 1/2$ is proposed in order to further improve the computational stability of the boundary treatment. In Section III, numerical results for four 3-D steady flows are examined and various computational issues are addressed. These four cases are: (i) pressure driven fully developed flow in a square duct; (ii) 3-D lid-driven cavity flow; (iii) pressure driven fully developed flow in a circular pipe; and (iv) uniform flow over a sphere. In cases (i) and (iii), the LBE-based numerical solutions can be compared with known exact solutions so that the accuracy of the LBE solutions can be determined. The difference in these two cases is that Δ is a constant in the square duct while Δ varies around the solid boundary in the circular pipe. In the lid-driven cavity flow, the singularities at corners between the moving and stationary walls allows for a performance assessment of various LBE schemes. The flow past a sphere is an external flow around a 3-D blunt body. In all four cases, detailed assessments are made in terms of error norms and velocity profiles. It will be demonstrated that accurate and robust solutions are obtained using the newly proposed boundary conditions along with the selected LBE models.

II. MODIFICATION OF THE BOUNDARY CONDITION FOR $\Delta > 1/2$

Equations (9)–(12) are first applied to a fully developed pressure driven 2-D channel flow by using the 3-D LBE model Q19D3. At the inlet ($i = 1$) and exit ($i = N_x$, in which N_x is the number of lattices in the x-direction) the following zero derivative condition is imposed after the collision step:

$$\tilde{f}_\alpha(i = 1, j, k) = \tilde{f}_\alpha(i = 2, j, k), \tag{13}$$

$$\tilde{f}_\alpha(i = N_x, j, k) = \tilde{f}_\alpha(i = N_x - 1, j, k). \tag{14}$$

At $k = 1$ and $k = N_z$, the same is imposed:

$$\tilde{f}_\alpha(i, j, k = 1) = \tilde{f}_\alpha(i, j, k = 2), \tag{15}$$

$$\tilde{f}_\alpha(i, j, k = N_z) = \tilde{f}_\alpha(i, j, k = N_z - 1). \tag{16}$$

The constant pressure gradient ∇p along the x-direction is treated as a body force and is included in the solution procedure after the collision step and the enforcement of the above

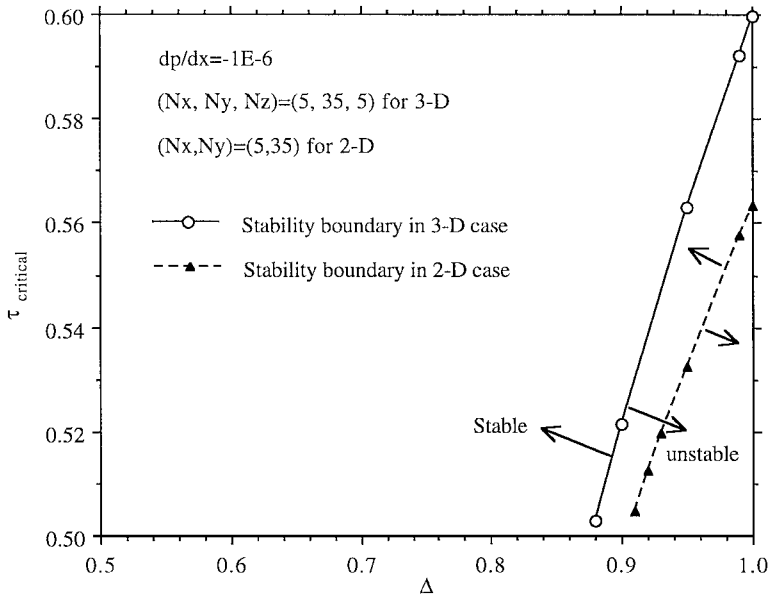

FIG. 2. Stability boundary of FHs scheme in a square duct flow for Δ near 1.

zero-derivative conditions as

$$\tilde{f}_\alpha(\boldsymbol{x}_i, t) = \tilde{f}_\alpha(\boldsymbol{x}_i, t) - w_\alpha \frac{3}{c^2}\frac{dp}{dx}\boldsymbol{e}_\alpha \cdot \hat{\mathbf{x}}, \tag{17}$$

where $\hat{\boldsymbol{x}}$ is the unit vector along the $\boldsymbol{x}$-axis. On the solid walls ($y = 0$ and $y = H$), Eqs. (9)–(12) are used. The exact solution for the velocity is used as the velocity initial condition. The equilibrium distribution function $f_\alpha^{(\mathrm{eq})}$ based on the exact solution for the velocity profile is used as the initial condition for f_α. The pressure gradient is set to $\frac{dp}{dx} = -1.0 \times 10^{-6}$. All computations are carried out using double precision.

It was found that the computations are stable for τ close to 0.5 (for example, $\tau = 0.505$) as long as Δ is not too close to unity (for example, $\Delta \leq 0.87$). When Δ is equal to 1, stable computation can only be carried out for τ no smaller than 0.6. Figure 2 shows the stability-instability boundary for the channel flow simulation with a system size $N_x \times N_y \times N_z = 5 \times 35 \times 5$, near $\Delta = 1$. Also shown by the dashed line is the stability–instability boundary for the channel flow simulation using the Q9D2 model and with a system size $N_x \times N_y = 5 \times 35$, near $\Delta = 1$. It is clear that similar behavior exists in both 2-D and 3-D channel flow simulations. When the computation for the pressure driven flow in a square duct was carried out using the Q19D3 formulation, a similar stability-instability boundary was encountered.

Ideally, one would like to use a fixed value of τ for the entire range of $0 \leq \Delta \leq 1$ in a simulation. Computational stability would then require the use of τ around 0.6, instead of a value that is close to 0.5, which makes it difficult to simulate a lower viscosity or higher Reynolds number flow. To overcome the restriction imposed by the numerical stability requirement due to interpolation, it would be useful if one could decrease the value of $\chi = (2\Delta - 1)/\tau$ given by Eq. (11). This can be accomplished by using

$$\boldsymbol{u}_{bf} = [1 - 3/(2\Delta)]\boldsymbol{u}_f + 3/(2\Delta)\boldsymbol{u}_w \quad \text{and} \quad \chi = (2\Delta - 1)/(\tau + 1/2) \qquad \text{for } \Delta \geq 1/2. \tag{18}$$

That is, the velocity $\boldsymbol{u}_{bf}$ is evaluated at $(\boldsymbol{x}_b + 1/2\,\boldsymbol{e}_\alpha)$, instead of at $\boldsymbol{x}_b$, using the information at $\boldsymbol{x}_f$ and $\boldsymbol{x}_w$ through linear extrapolation.

With Eq. (18) replacing Eq. (11), the channel flow simulations using the Q19D3 lattice model are carried out again for Δ from 0.85 to 1. Satisfactory results for the velocity profiles are obtained for $\tau = 0.505$ with $N_x \times N_y \times N_z = 5 \times 35 \times 5$ in terms of computational stability. For $\Delta < 0.85$, the accuracy of the solutions using Eqs. (11) and (18) is the same when the computations are stable.

III. RESULTS AND DISCUSSIONS

3.1. *Fully Developed Flow in a Square Duct*

For fully developed flow inside a square duct of height H defined by the region $-a \le y \le a$ and $-a \le z \le a$, where $a = H/2$, the axial velocity profile can be found in Ref. [24, p. 123]:

$$u_x(y, z) = -\frac{16a^2}{\mu\pi^3}\frac{dp}{dx}\sum_{n=1,3,5,\ldots}^{\infty}\left[1 - \frac{\cosh(n\pi z/2a)}{\cosh(n\pi/2)}\right]\frac{\cos(n\pi y/2a)}{n^3}. \tag{19}$$

Figure 3 compares the exact axial velocity profiles at $z = 0$ and the LBE-based solution with $\Delta = 0.2$ and $H = 2a = 32.4$. A total of $N_x \times N_y \times N_z = 13 \times 35 \times 35$ grid points are used. The pressure gradient is $\frac{dp}{dx} = -1.0 \times 10^{-6}$ and $\tau = 0.52$. The 19-bit model is used in the simulations. Excellent agreement was obtained.

Figure 4a shows the dependence of relative L_2-norm error,

$$E_2 = \frac{\left\{\int_0^H \int_0^H [u_{\mathrm{LBE}}(y, z) - u_{\mathrm{exact}}(y, z)]^2\, dy\, dz\right\}^{1/2}}{\left[\int_0^H \int_0^H u_{\mathrm{exact}}^2(y, z)\, dy\, dz\right]^{1/2}}, \tag{20}$$

on the duct height or the lattice resolution $H = N_y - 3 + 2\Delta$. The integral is evaluated by

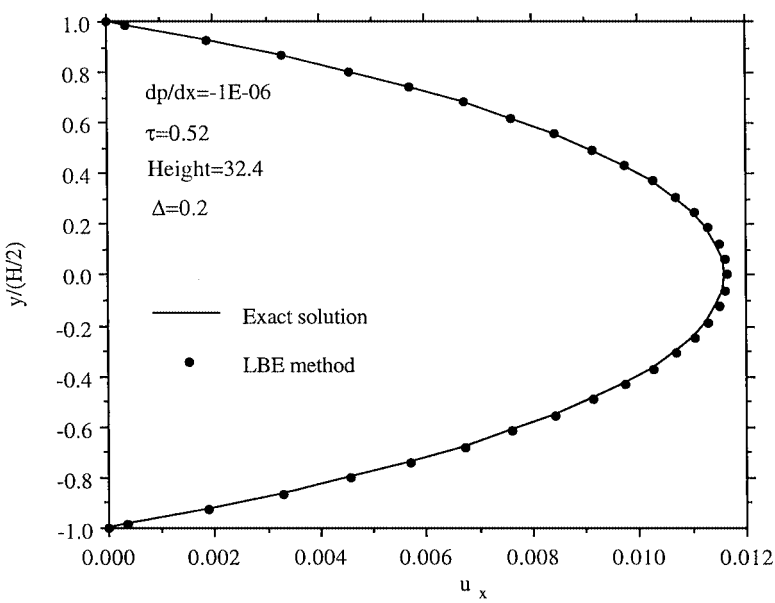

FIG. 3. Comparison of axial velocity profiles in a pressure driven square duct flow at $z = 0$ between the exact solution and the LBE-based solution with $\Delta = 0.2$.

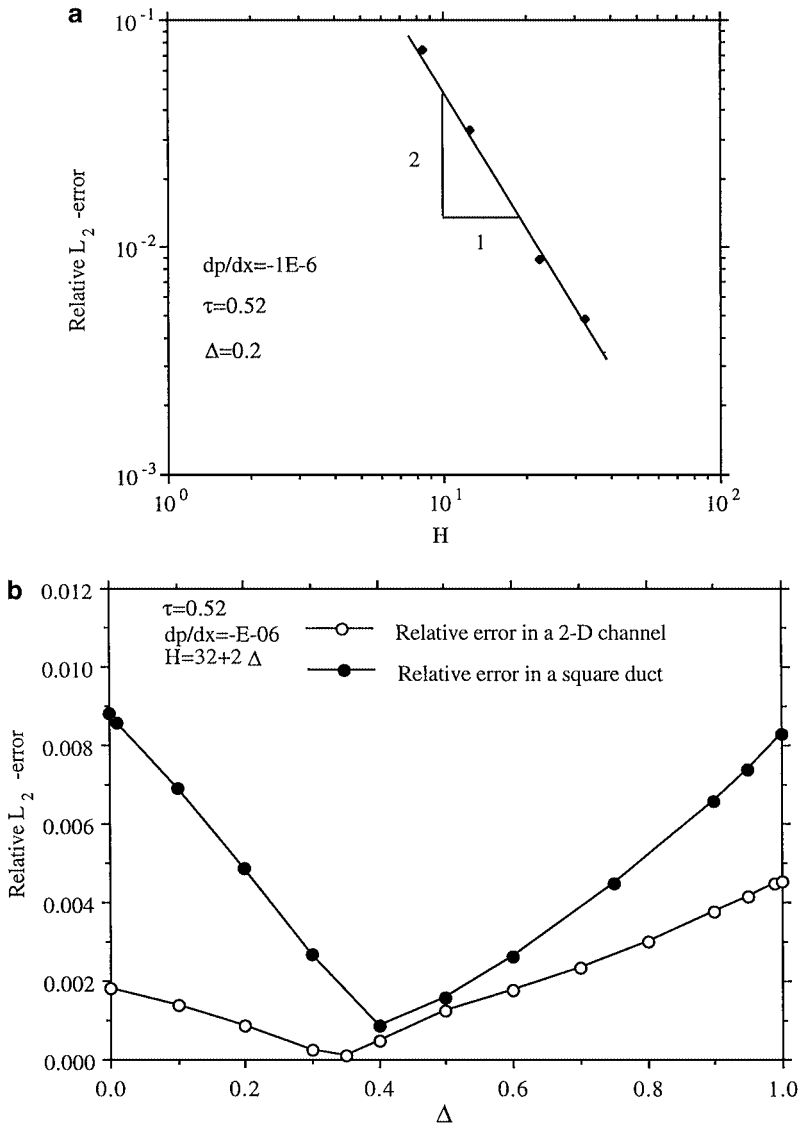

FIG. 4. (a) Dependence of relative L_2-norm error on the lattice resolution $H = N_y - 3 + 2\Delta$ in steady state pressure-driven duct flow simulations. (b) Relative L_2-norm error as a function of Δ in steady-state pressure-driven duct and channel flow simulations.

the trapezoidal rule. As was demonstrated by Mei *et al.* [22], the boundary treatment results in second order convergence for 2-D channel flow. Figure 4a clearly shows that the total error (from both the flow field and the boundary condition) of the LBE solution in 3-D flow decays quadratically.

Figure 4b shows the relative L_2-norm error E_2 as a function of Δ in the duct flow using $13 \times 35 \times 35$ grid points and $\tau = 0.52$. For the purpose of comparison, the relative L_2-norm error in the 2-D channel flow simulation using the Q9D2 model with $N_y = 35$ and $\tau = 0.52$ is also shown. The relative error is larger in 3-D duct flow than in the 2-D channel flow. Nevertheless, the error exhibits the same qualitative behavior in both 2-D and 3-D as a function of Δ.

It should be noted that the accuracy of the Q9D2 model and the Q19D3 model is different in the sense that beyond the conserved moments (density and momentum in athermal fluids), these two models have different accuracy in preserving higher order moments (fluxes) [9, 10]. The Q9D2 model preserves all the moments up to second order in momentum space, which include momentum fluxes, and maintains the isotropy of these moments, whereas the Q19D3 model can preserve density and momentum, but cannot maintain the same accuracy and isotropy of the fluxes like the Q9D2 model does. The only 3-D equivalent of the Q9D2 model in terms of accuracy of the moments is the Q27D3 model [9, 10].

3.2. *Simulation Results for 3-D Lid-Driven Cavity Flows*

Lid-driven cavity flow has been studied extensively in the CFD community. Most research has been focused on 2-D problems. Limited numbers of reliable numerical results for steady state 3-D cavity flows have been obtained in the past several years. In this study, the multiblock finite difference solution of the NS equations obtained recently by Salom [25] is used to compare with the present LBE-based results.

The size of the cavity is H^3, the number of grids is $N_x \times N_y \times N_z$, and $N_x = N_y = N_z$. The driving lid is placed at $y = H$, moving along the direction of x-axis with a speed $U = 0.1$ in lattice units. Figure 5a compares profiles of horizontal velocity $u_x(y)$ obtained using $33 \times 33 \times 33$ lattices with the solution to the NS equations at $x/H = z/H = 0.5$ for $Re = 400$. All three LBE models (15-, 19-, and 27-bit) are used. For the 15-bit model, the computation becomes unstable and blows up at this Reynolds number with 33^3 lattice resolution and $\Delta = 0.5$. For $\Delta = 0.5$, the 19- and the 27-bit models give very similar $u_x(y)$ profiles and both underpredict slightly the magnitude of the minimum in the profiles. The 19-bit model is also used with $\Delta = 0.25$; there is a slight overshoot in the velocity profiles in comparison to the results in Ref. [25]. Figure 5b compares $u_x(y)$ profiles obtained using the 15- and 19-bit lattice models on the 67^3 lattice grids and $\Delta = 0.5$ with the NS solution [25] at $x/H = z/H = 0.5$ for $Re = 400$. Excellent agreement is observed. Clearly, the 19-bit model is superior to the 15-bit model. Although the 15-bit model requires 21% less CPU time and storage than the 19-bit model per lattice, it is not as robust as the 19-bit model and may actually require more CPU time and memory to obtain a reasonable solution since more lattice points are clearly needed.

It should be noted that the stability property of the 19- and the 15-bit models is significantly different. All LBE models have inherent spurious invariants because of their simple dynamics [30]. However, the stability of the LBE models, which is very much affected by these spurious invariants, differs from one model to another and also depends on other factors such as boundary conditions and the local Reynolds number [30]. Among the three 3-D LBE models (Q15D3, Q19D3, and D27D3), the Q15D3 model is the least isotropic and therefore is more prone to numerical instability. This is independently verified in a recent work by Kandhai *et al.* [26]. It was observed that the Q15D3 model may induce artificial checkerboard invariants which are the eigenmodes of the linearized LBGK collision operator at wave vector $k = \pi$; this can cause spatial oscillations to develop in the flow field at high Reynolds number [30]. Although it was pointed out that the presence of solid walls can suppress the oscillation in certain cases, the solid walls in the present case actually excite the oscillation by producing shear stress singularities at the corners between the moving and the stationary walls. Clearly, the Q19D3 model is better suited to handle flow singularities than the Q15D3 model in this case.

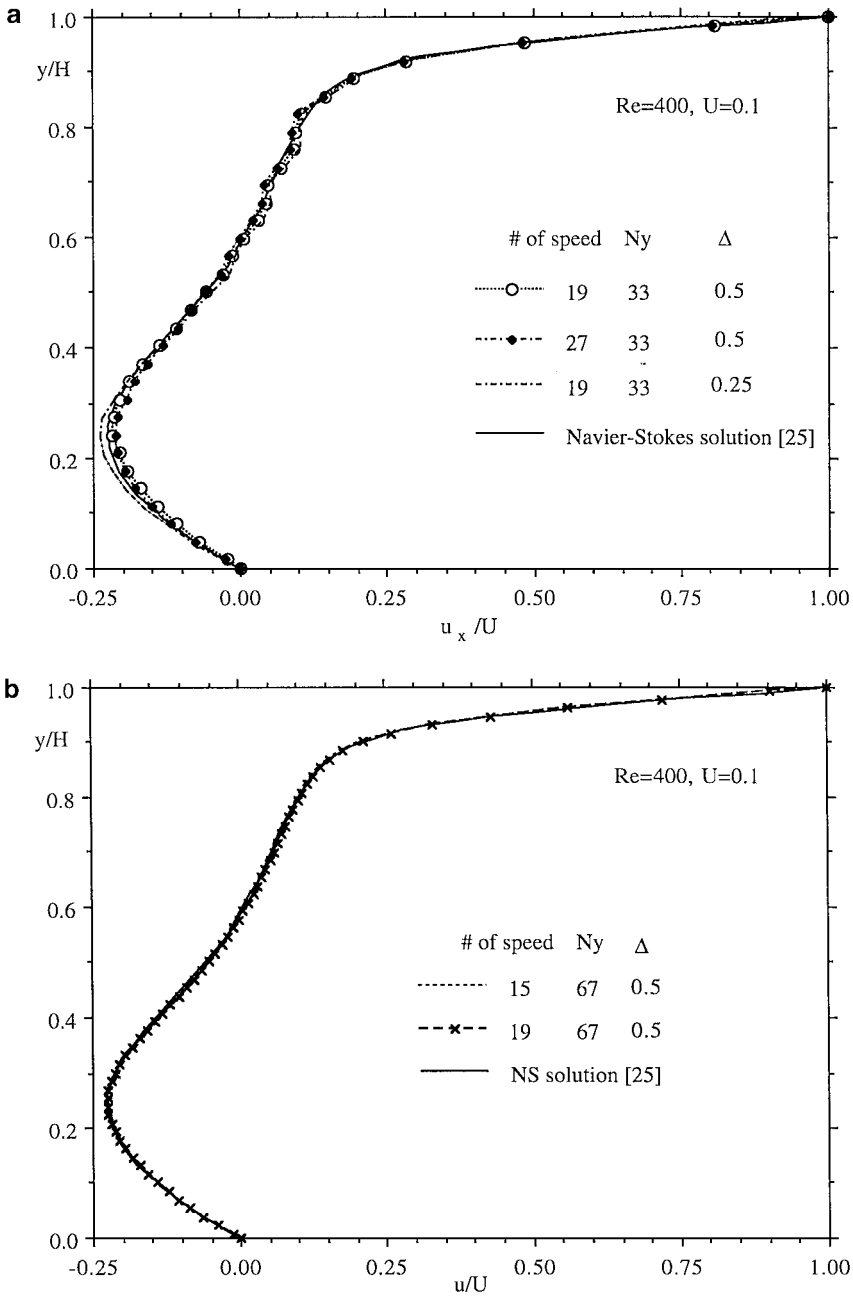

FIG. 5. Comparison of u_x profiles using (a) $33 \times 33 \times 33$ and (b) $67 \times 67 \times 67$ lattices with a Navier–Stokes (NS) solution at $x/H = z/H = 0.5$ for $Re = 400$ in a lid-driven cavity flow.

Figure 6a compares the profiles of transversal velocity $u_y(x)$ obtained from various 3-D LBE models using 33^3 lattices (grids) with the NS solution at $y/H = z/H = 0.5$ for $Re = 400$. For $\Delta = 0.5$, we found that the results from the 27-bit model deviate more from the NS results of Ref. [25] than the results of the 19-bit model with the same resolution in the spatial region $0.1 < x/H < 0.6$. Both models underpredict the extrema of the velocity profile compared to the NS solution of Ref. [25]. For $\Delta = 0.25$, the results of the 19-bit

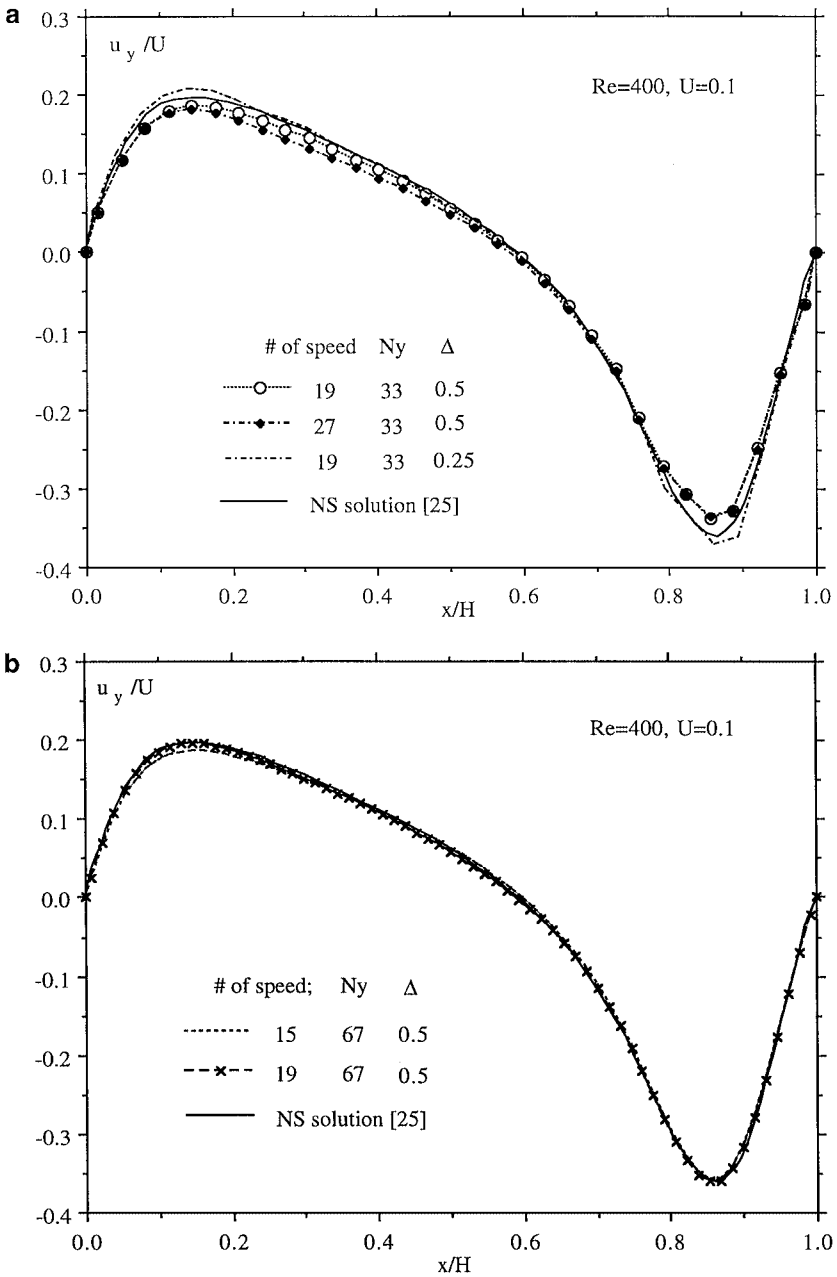

FIG. 6. Comparison of u_y profiles using (a) $33 \times 33 \times 33$ and (b) $67 \times 67 \times 67$ lattices with an NS solution at $y/H = z/H = 0.5$ for $Re = 400$ in a lid-driven cavity flow.

model slightly overpredict the extrema, also shown in Fig. 6a. However, the difference is relatively smaller in both cases. Figure 6b shows velocity profiles with a resolution of 67^3 grid points and the same Reynolds number $Re = 400$. With 67^3 lattice resolution, the result of the 15-bit model significantly differs from the results of the 19-bit model and that of the NS solution in Ref. [25]. These comparisons further suggest that the 19-bit model is better than the 15-bit model in terms of accuracy and stability and better than the 27-bit in terms

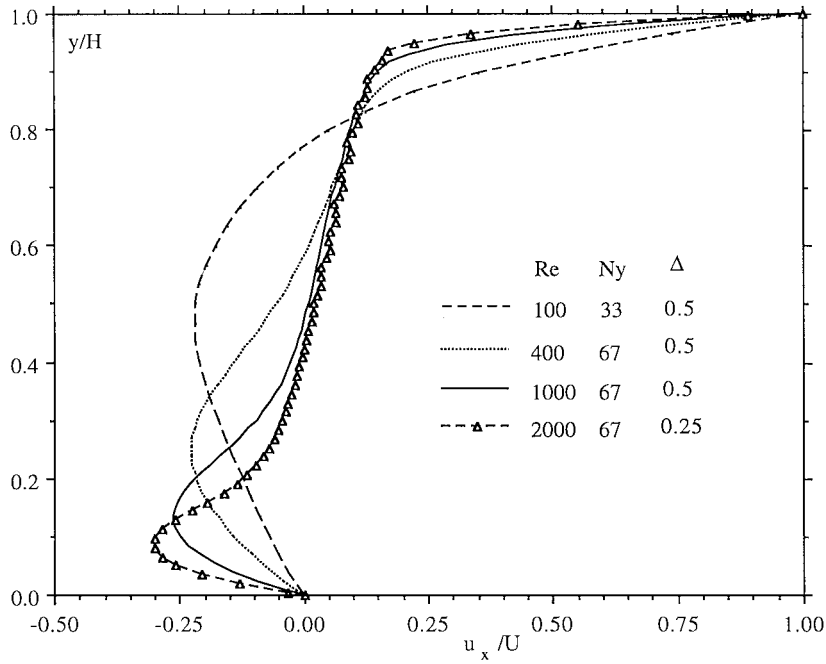

FIG. 7. Effect of Reynolds number on the centerline ($x/H = z/H = 1/2$) velocity profiles, u_x/U, based on the 19-bit LBE solutions in a lid-driven cavity flow.

of computational efficiency. The 19-bit model represents a good compromise in terms of both computational efficiency and reliability.

Figures 7 and 8 show the effect of Reynolds number (from 100 to 2000) on the profiles of horizontal velocity $u_x(y)$ at $x/H = z/H = 0.5$ and transversal velocity $u_y(x)$ at $y/H = z/H = 0.5$ based on the Q19D3 model. For $Re = 100$, 400, and 1000, $\Delta = 0.5$ is used. It is worth noting that for $Re = 2000$, the system size of 67^3, $U = 0.1$, and $\tau = 0.50325$, the LBE simulation with $\Delta = 0.5$ eventually becomes unstable, although the steady-state result of $Re = 1000$ is used as the initial condition for $Re = 2000$. When $\Delta = 0.25$ is used on the 67^3 lattice system, no computational instability occurs and the steady-state solution is obtained. Weak spatial oscillations in the $u_x(y)$ and $u_y(x)$ velocity profiles were observed for $Re = 2000$, which indicates that further increase in Re would require better spatial resolution. It is also worth pointing out that when FH's boundary condition [23] is used for $Re = 2000$ with $\Delta = 0.25$, the solution eventually blows up even when converged results (based on the present boundary condition for $\Delta = 0.25$) at $Re = 2000$ are used as the initial condition.

3.3. *Fully Developed Flows inside a Circular Pipe*

Figure 9 shows the 2-D projection of the discretized domain and the boundary nodes $\boldsymbol{x}_b$ (denoted by solid symbols) on the yz plane for flow inside a circular pipe of radius $R = 9.5$ lattice units. Geometrically, the LBE simulation of the pipe flow differs from that of the duct flow in that the fraction of the intersected link Δ is not constant over the entire boundary. As seen in Fig. 4b, computational error can vary with Δ in the duct flow and the difference in the error can easily be as large as a factor of four for $0 \le \Delta \le 1$. Furthermore, the error is the smallest when Δ is between 0.3 to 0.6. Hence, it is reasonable to expect that the overall error in the solution will depend on the distribution of Δ in the entire set of Δ.

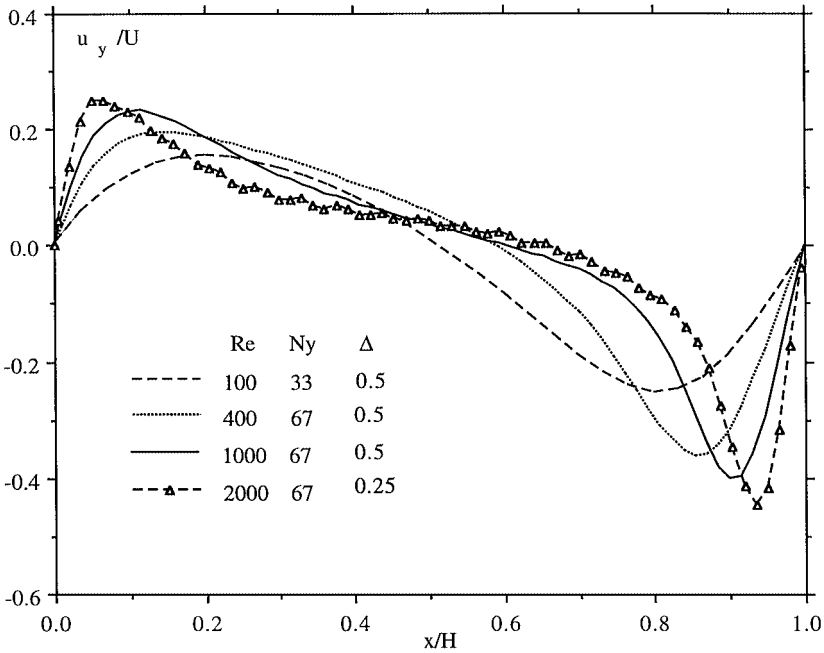

FIG. 8. Effect of Reynolds number on the y-component velocity profiles at $y/H = z/H = 1/2$ based on the 19-bit LBE solutions in a lid-driven cavity flow.

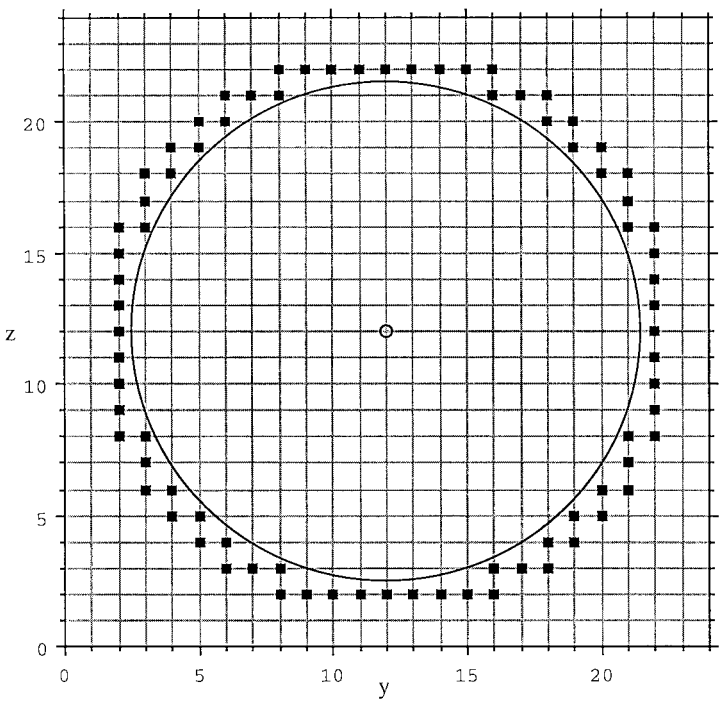

FIG. 9. Boundary nodes $\mathbf{x}_b$ (solid symbols) for flow in a pipe of radius 9.5 lattice units.

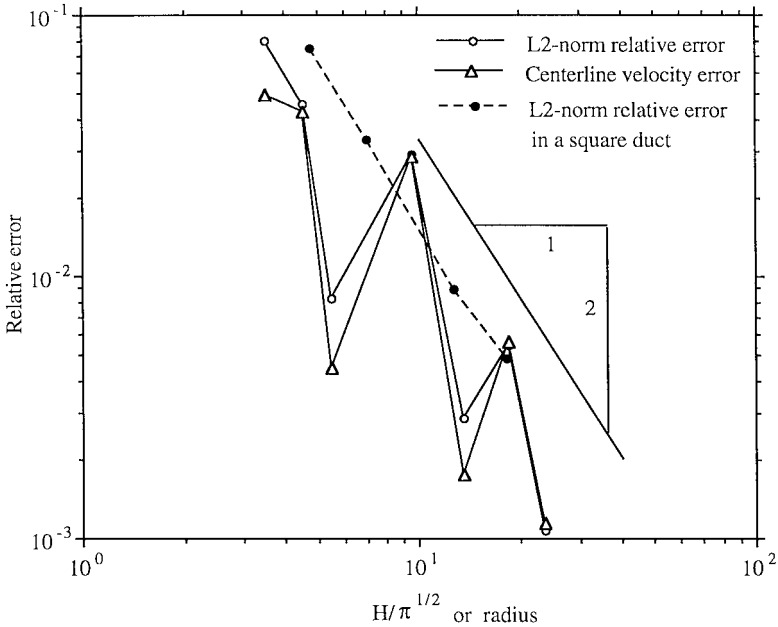

FIG. 10. Variation of relative errors in the velocity profiles as a function of pipe radius.

Figure 10 shows the relative L_2-norm error for the axial velocity profile defined as

$$E_2 = \frac{\left\{\sum_{(y_j,z_k)\in\Omega}[u_{\mathrm{LBE}}(y_j,z_k) - u_{\mathrm{exact}}(y_j,z_k)]^2\right\}^{1/2}}{\left[\sum_{(y_j,z_k)\in\Omega} u^2_{\mathrm{exact}}(y_j,z_k)\right]^{1/2}}, \tag{21}$$

where Ω is the set of the discrete lattice grids inside the pipe, as a function of radius R for $R = 3.5$, 4.5, 5.5, 9.5, 13.5, 18.5, and 23.5. The pressure gradient is $\frac{dp}{dx} = -1.0 \times 10^{-6}$ and $\tau = 0.52$. It is noted that each simple summation in Eq. (21) is slightly less than the exact integration over the entire circle due to the discretization. To ensure that such a treatment does not affect the qualitative behavior of the error measurement, the centerline axial velocity, u_c, is also compared with the exact solution and the error is defined as:

$$E_c = \frac{|u_{c,\mathrm{LBE}} - u_{c,\mathrm{exact}}|}{|u_{c,\mathrm{exact}}|}. \tag{22}$$

It is seen that E_c behaves very similarly to E_2 and both are nonmonotonic. This oscillatory behavior could be due to the difference in the distribution of Δ, which in turn results in the difference of the dissipation due to the interpolation around the boundary. Shown also in Fig. 10 is the error E_2 of the square duct flow solution (with $\Delta = 0.2$) as a function of equivalent radius $H/\pi^{1/2}$, which exhibits a quadratic convergence. Despite the nonmonotonic behavior, it can still be seen that on average, E_2 and E_c decay quadratically with increasing radius and the accuracy in the pipe flow simulation is comparable to that in the square duct flow simulation.

Figure 11 shows the axial velocity profiles in the pipe for $R = 3.5$, 5.5, 9.5, and 13.5 in comparison with the exact solution. Even for a very small radius $R = 3.5$, the LBE solution agrees with the exact solution remarkably well. A noticeable discrepancy in the velocity profile at $R = 9.5$ is also observed in E_2 and E_c shown in Fig. 10.

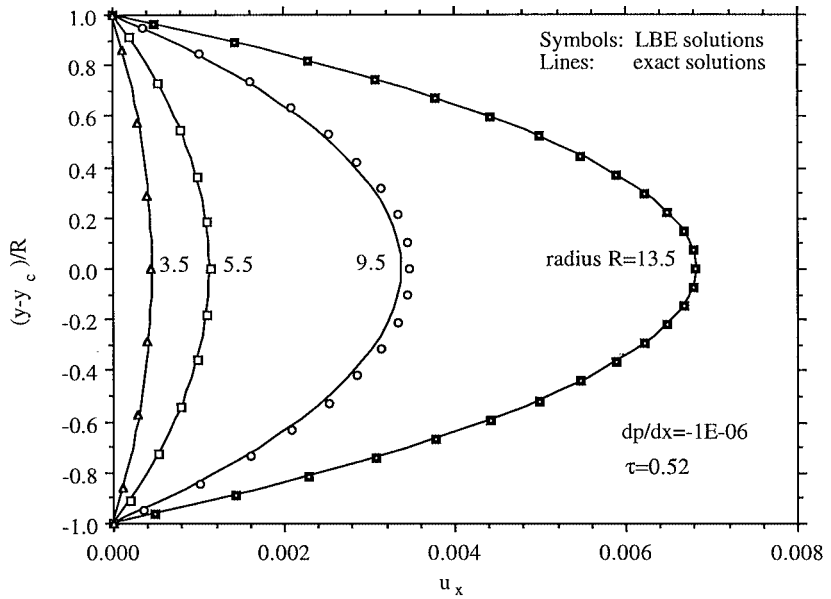

FIG. 11. Comparison of the axial velocity profiles between the LBE-based and the exact solutions for flow inside a cicular pipe.

3.4. *Simulation Results for a Uniform Flow over a Sphere*

The conventional LBE scheme uses uniform meshes. Without local mesh refinement, it is difficult to compute the external flow over a blunt body efficiently since a large number of grid points in the far field will be wasted. As a first attempt, the flow over a sphere is computed within a finite region in the transversal directions.

As shown in Fig. 12, the outer boundary is placed at $y = \pm H/2$ and $z = \pm H/2$. At $y = -H/2$, the lattice is $j = 2$. The boundary conditions at $j = 1$ for f_α's are given by the following linear extrapolation:

$$f_\alpha(i, 1, k) = 2 f_\alpha(i, 2, k) - f_\alpha(i, 3, k). \tag{23}$$

The velocity at $j = 2$ is set as

$$\boldsymbol{u}(i, 2, k) = \boldsymbol{u}(i, 3, k). \tag{24}$$

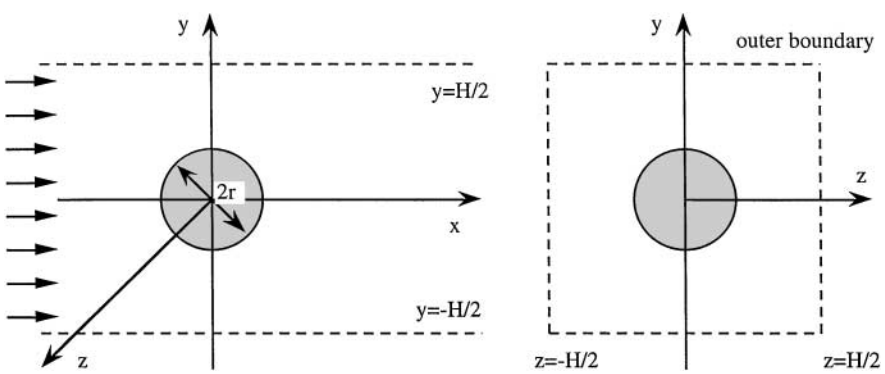

FIG. 12. Schematic for uniform flow over a sphere.

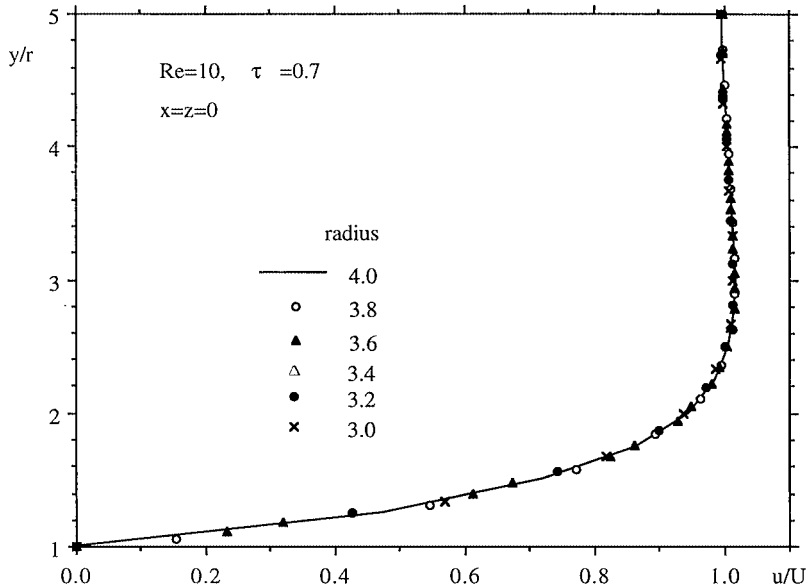

FIG. 13. Comparison of the velocity profiles at $x = 0$ for $r = 3.0$, 3.2, 3.4, 3.6, 3.8, and 4.0 for $Re = 10$ and $H/r = 5$.

Similar treatment is applied at $y = H/2$ and $z = \pm H/2$. The extrapolation condition given by Eqs. (23) and (24) allow the flow to leave the outer boundary. This helps to reduce the effect of the outer boundary on the flow field and on the drag force. At the inlet, a uniform velocity profile is imposed at $i = 1.5$ (halfway between the first and second lattice points) and Eq. (9) is applied to obtain the condition for $f_\alpha(1, j, k)$ with $\chi = 0$. At the exit, a simple extrapolation is used:

$$f_\alpha(N_x, j, k) = 2 f_\alpha(N_x - 1, j, k) - f_\alpha(N_x - 2, j, k). \tag{25}$$

On the surface of the sphere, Eqs. (9), (10), (12), and (18) proposed in this work are used to update the boundary conditions for f_α's. Only the 19-bit LBE model is used to simulate the flow over a sphere.

Figure 13 shows the velocity profile $u_x(y)$ based on a series of computations carried out for several values of the radius $R = 3.0$, 3.2, 3.4, 3.6, 3.8, and 4.0 for $H/R = 10$ at $Re = 10$. The results are obtained with $\tau = 0.7$. Figure 14 compares the axial velocity profile (at $y = z = 0$) for the same set of parameters. It is worth noting that the present LBE computation does not have sufficient resolution for the given Reynolds number. Yet the velocity profiles agree with each other accurately. The fact that we have obtained a spatially accurate solution over a range of radii strongly suggests that the present boundary condition treatment for curved geometry in the LBE method is capable of handling more complex geometries while maintaining good accuracy.

VI. CONCLUDING REMARKS

Three 3-D LBE models, including the 15-, 19-, and 27-bit models, have been assessed in terms of efficiency, accuracy, and robustness in lid-driven cavity flow. While accurate 3-D results can be obtained by using various LBE models, the 19-bit model is found to be the

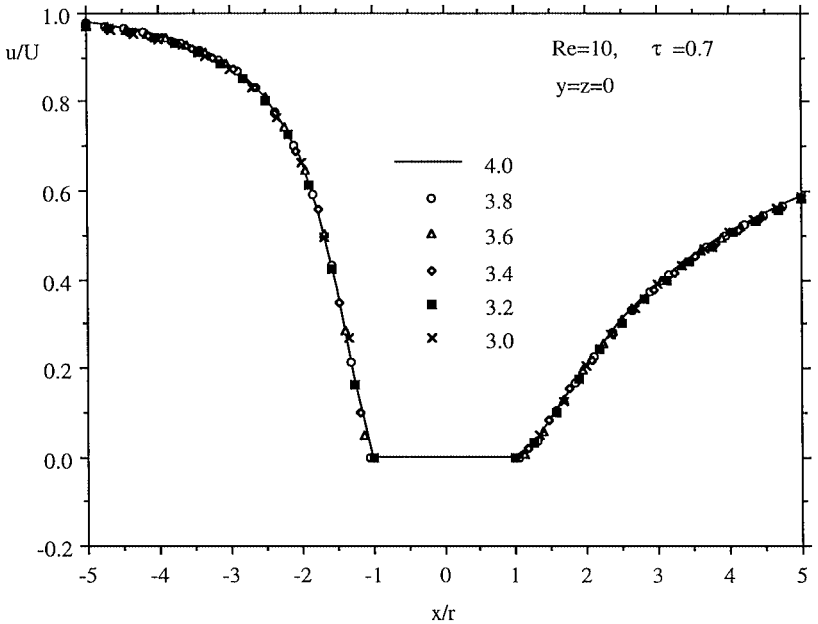

FIG. 14. Comparison of the centerline velocity ($y = 0$) for $r = 3.0$, 3.2, 3.4, 3.6, 3.8, and 4.0 for $Re = 10$ and $H/r = 5$.

best for the cases investigated. The 15-bit model exhibits velocity oscillations and is prone to computational instability. The more complicated 27-bit model does not necessarily give more accurate results than the 19-bit model with the same spatial resolution.

In this study, we have also modified the boundary condition treatment for the LBE method proposed by Filippova and Hänel [23] and Mei *et al.* [22] when the fraction of the intersected link on the boundary Δ is greater than one half. This improves the computational stability when Δ is close to 1 and τ close to $1/2$.

The simulations for flows in a square duct and in a circular pipe indicate that the current boundary condition treatment for curved geometries results in second-order accuracy in 3-D flows. The velocity profiles for flow over a sphere show good self-consistency of the solution over a range of sphere radii used.

APPENDIX

The Q15D3 model has the following set of discrete velocities:

$$\boldsymbol{e}_\alpha = \begin{cases} (0, 0, 0), & \alpha = 0; \text{ rest particle} \\ (\pm 1, 0, 0)c, (0, \pm 1, 0)c, (0, 0, \pm 1)c, & \alpha = 1, 2, \ldots, 6; \text{ group I} \\ (\pm 1, \pm 1, \pm 1)c, & \alpha = 7, 8, \ldots, 14; \text{ group III} \end{cases} \tag{A1}$$

and the weighting factor w_α is [12]

$$w_\alpha = \begin{cases} 2/9, & \alpha = 0; \text{ rest particle} \\ 1/9, & \alpha = 1, 2, \ldots, 6; \text{ group I} \\ 1/72, & \alpha = 7, 8, \ldots, 14; \text{ group III.} \end{cases} \tag{A2}$$

The Q19D3 model has the following set of discrete velocities:

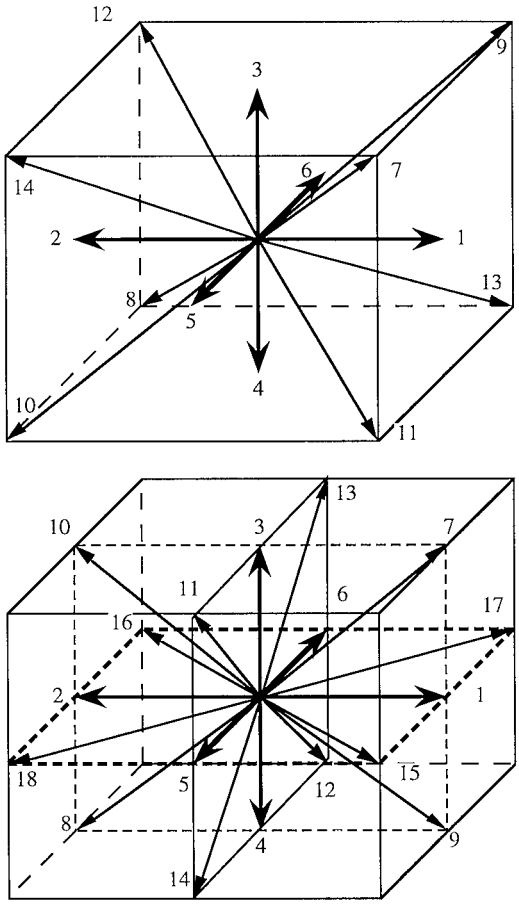

FIG. A1. Discrete velocity vectors for the Q15D3 and Q19D3 lattices.

$$\boldsymbol{e}_\alpha = \begin{cases} (0,0,0), & \alpha = 0, \text{ rest particle} \\ (\pm 1,0,0)c,\ (0,\pm 1,0)c,\ (0,0,\pm 1)c, & \alpha = 1,2,\ldots,6; \text{ group I} \\ (\pm 1,\pm 1,0)c,\ (\pm 1,0,\pm 1)c,\ (0,\pm 1,\pm 1)c, & \alpha = 7,8,\ldots,18; \text{ group II} \end{cases} \tag{A3}$$

and the weighting factor w_α is [9]

$$w_\alpha = \begin{cases} 1/3, & \alpha = 0; \text{ rest particle} \\ 1/18, & \alpha = 1,2,\ldots,6; \text{ group I} \\ 1/36, & \alpha = 7,8,\ldots,18; \text{ group II.} \end{cases} \tag{A4}$$

The Q27D3 model has the following discrete velocities:

$$\boldsymbol{e}_\alpha = \begin{cases} (0,0,0), & \alpha = 0; \text{ rest particle} \\ (\pm 1,0,0)c,\ (0,\pm 1,0)c,\ (0,0,\pm 1)c, & \alpha = 1,2,\ldots,6; \text{ group I} \\ (\pm 1,\pm 1,0)c,\ (\pm 1,0,\pm 1)c,\ (0,\pm 1,\pm 1)c, & \alpha = 7,8,\ldots,18; \text{ group II} \\ (\pm 1,\pm 1,\pm 1)c, & \alpha = 19,20,\ldots,26; \text{ group III} \end{cases} \tag{A5}$$

and the weighting factor w_α is [9]

$$w_\alpha = \begin{cases} 8/27, & \alpha = 0, \text{ rest particle} \\ 2/27, & \alpha = 1, 2, \ldots, 6; \text{ group I} \\ 1/54, & \alpha = 7, 8, \ldots, 18; \text{ group II} \\ 1/216, & \alpha = 19, 20, \ldots, 26; \text{ group III.} \end{cases} \tag{A6}$$

In the above, $c = \delta x/\delta t$, δx and δt are the lattice constant and the time step size, respectively. The lattice structures for the Q15D3 and Q19D3 models are shown in Fig. A1.

ACKNOWLEDGMENTS

This work is partially supported by NASA Langley Research Center under the program of Innovative Algorithms for Aerospace Engineering Analysis and Optimization. R. Mei also acknowledges partial support of the Engineering Research Center (ERC) for Particle Science & Technology at the University of Florida, the National Science Foundation (EEC-9402989), and Industrial partners of the ERC. W. Shyy acknowledges partial support of AFOSR and Eglin AFB. We thank Dr. O. Filippova and Prof. D. Hänel for helpful discussions and are grateful to Dr. R. Rubinstein for his careful reading of the manuscript.

REFERENCES

1. R. Peyret and T. D. Taylor, *Computational Technique for Fluid Dynamics*, Vol. II (Springer-Verlag, New York, 1983).
2. C. A. J. Fletcher, *Computational Techniques for Fluid Dynamics*, Vols. I & II (Springer-Verlag, New York, 1988).
3. W. Shyy, *Computational Modeling for Fluid Flow and Interfacial Transport*, Corrected printing (Elsevier, Amsterdam, 1997).
4. H. Chen, S. Chen, and W. H. Matthaeus, Recovery of the Navier–Stokes equations using a lattice–gas Boltzmann method, *Phys. Rev. A* **45**, R5339 (1992).
5. Y. H. Qian, D. d'Humières, and P. Lallemand, Lattice BGK models for Navier–Stokes equation, *Europhys. Lett.* **17**, 479 (1992).
6. R. Benzi, S. Succi, and M. Vergassola, The lattice Boltzmann equation: Theory and applications, *Phys. Rep.* **222**, 145 (1992).
7. S. Chen and G. D. Doolen, Lattice Boltzmann method for fluid flows, *Ann. Rev. Fluid Mech.* **30**, 329 (1998).
8. X. He and L.-S. Luo, *A priori* derivation of the lattice Boltzmann equation, *Phys. Rev. E* **55**, R6333 (1997).
9. X. He and L.-S. Luo, Theory of the lattice Boltzmann method: From the Boltzmann equation to the lattice Boltzmann equation, *Phys. Rev. E* **56**, 6811 (1997).
10. T. Abe, Derivation of the lattice Boltzmann method by means of the discrete ordinate method for the Boltzmann equation, *J. Comput. Phys.* **131**, 241 (1997).
11. P. L. Bhatnagar, E. P. Gross, and M. Krook, A model for collision processes in gases. I. Small amplitude processes in charged and neutral one-component system, *Phys. Rev. A* **94**, 511 (1954).
12. Y. H. Qian, S. Succi, and S. A. Orszag, Recent advances in lattice Boltzmann computing, in *Annual Reviews of Computational Physics*, Vol. III (D. Stauffer, Ed., World Scientific, Singapore), pp. 195–242 (1995).
13. D. P. Ziegler, Boundary conditions for lattice Boltzmann simulations, *J. Stat. Phys.* **71**, 1171 (1993).
14. I. Ginzbourg and P. M. Alder, Boundary flow condition analysis for the three-dimensional lattice Boltzmann model, *J. Phys. II France* **4**, 191 (1994).
15. X. He, Q. Zou, L.-S. Luo, and M. Dembo, Analytic solutions and analysis on non-slip boundary condition for the lattice Boltzmann BGK model, *J. Stat. Phys.* **87**, 115 (1997).
16. O. Behrend, Solid boundaries in particle suspension simulations via lattice Boltzmann method, *Phys. Rev. E* **52**, 1164 (1995).

17. L.-S. Luo, Analytic solutions of linearized lattice Boltzmann equation for simple flows, *J. Stat. Phys.* **88**, 913 (1997).
18. A. J. C. Ladd, Numerical simulation of particular suspensions via a discretized Boltzmann equation, Part 2, Numerical results, *J. Fluid Mech.* **271**, 311 (1994).
19. D. R. Noble, S. Chen, J. G. Georgiadis, and R. O. Buckius, A consistent hydrodynamic boundary condition for the lattice Boltzmann method, *Phys. Fluid* **7**, 203 (1995).
20. S. Chen, D. Martinez, and R. Mei, On boundary conditions in lattice Boltzmann method, *Phys. Fluids* **8**, 2527 (1996).
21. Q. Zou and X. He, On pressure and velocity boundary conditions for the lattice Boltzmann BGK model, *Phys. Fluids* **9**, 1591 (1997).
22. R. Mei, L.-S. Luo, and W. Shyy, An accurate curved boundary treatment in the lattice Boltzmann method, *J. Comp. Phys.* **155**, 307 (1999).
23. O. Filippova and D. Hänel, Grid refinement for lattice-BGK models, *J. Comp. Phys.* **147**, 219 (1998).
24. F. M. White, *Viscous Fluid Flow* (McGraw-Hill, New York, 1974).
25. J. Salom, *Numerical Simulation of Convection Phenomena Based on Domain Decomposition Techniques and Experimental Validation*, Ph.D. dissertation, Universitat Politecnica de Catalunya, Spain (1999).
26. D. Kandhai, A. Koponen, A. Hoekstra, M. Kataja, J. Timonen, and P. M. A. Sloot, Implementation aspects of 3D lattice-BGK: boundaries, accuracy, and a new fast relaxation method, *J. Comp. Phys.* **150**, 482 (1999).
27. I. Ginzbourg and D. d'Humieres, Local second-order boundary methods for lattice Boltzmann models, *J. Stat. Phys.* **84**, 927 (1996).
28. R. Mei and W. Shyy, On the finite difference-based lattice Boltzmann method in curvilinear coordinates, *J. Comp. Phys.* **143**, 426 (1998).
29. X. He and G. Doolen, Lattice Boltzmann method on curvilinear coordinates systems: Flow around a circular cylinder, *J. Comp. Phys.* **134**, 306 (1997).
30. P. Lallemand and L.-S. Luo, Theory of the lattice Boltzmann method: Dispersion, dissipation, isotropy, Galilean invariance, and stability, *Phys. Rev. E*, to appear (2000).